










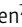


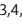




BRIEF DEFINITIVE REPORT

Helminth-induced reprogramming of the stem cell compartment inhibits type 2 immunity

Danielle Karo-Atar^{1,8,9} , Shaida Ouladan^{2,9} , Tanvi Javkar^{2,9} , Loick Joumier^{3,4} , Macy K. Matheson⁵ , Sydney Merritt¹ , Susan Westfall¹ , Annie Rochette^{2,9} , Maria E. Gentile¹ , Ghislaine Fontes¹ , Gregory J. Fonseca⁶ , Marc Parisien⁷ , Luda Diatchenko⁷ , Jakob von Moltke⁵ , Mohan Malleshaiah^{3,4,9} , Alex Gregorieff^{2,9} , and Irah L. King^{1,8,9} 

Enteric helminths form intimate physical connections with the intestinal epithelium, yet their ability to directly alter epithelial stem cell fate has not been resolved. Here we demonstrate that infection of mice with the parasite *Heligmosomoides polygyrus bakeri* (*Hpb*) reprograms the intestinal epithelium into a fetal-like state marked by the emergence of *Clusterin*-expressing revival stem cells (revSCs). Organoid-based studies using parasite-derived excretory-secretory products reveal that *Hpb*-mediated revSC generation occurs independently of host-derived immune signals and inhibits type 2 cytokine-driven differentiation of secretory epithelial lineages that promote their expulsion. Reciprocally, type 2 cytokine signals limit revSC differentiation and, consequently, *Hpb* fitness, indicating that helminths compete with their host for control of the intestinal stem cell compartment to promote continuation of their life cycle.

Introduction

Intestinal helminths remain pervasive throughout the animal kingdom by manipulating host defense pathways to prioritize tissue adaptation and repair over parasite expulsion (King and Li, 2018). This host defense strategy begins at the gut epithelium, a monolayer of cells continually replenished by intestinal stem cells (ISCs) residing at the crypt base. As frontline effectors of barrier integrity, a key attribute of the ISC compartment is its ability to undergo extensive transcriptional reprogramming in response to injury (Santos et al., 2018; de Sousa e Melo and de Sauvage, 2019). During homeostasis, ISCs, marked by the expression of leucine rich repeat containing G protein-coupled receptor 5 (*Lgr5*), reside at the crypt base where they are supported by growth factor-secreting Paneth cells and various stromal cell subsets (Clevers, 2013). In this setting, ISCs are responsible for the perpetual turnover of the entire repertoire of gut epithelial cell lineages (Clevers, 2013). In response to diverse forms of damage, *Lgr5*⁺ ISC are depleted but rapidly replenished, at least in part, by dedifferentiation of lineage-committed cells to swiftly regenerate the intestinal barrier (Meyer et al., 2022; Ouladan and Gregorieff, 2021; Larsen and Jensen, 2021). These

cell fate changes are often accompanied by upregulation of genes normally restricted to the fetal gut, suggesting that replenishment of stem cells following injury requires the temporary reversion or reprogramming of the adult gut epithelium into an embryonic state (Yui et al., 2018; Ohara et al., 2022). Indeed, we have recently identified a damage-induced ISC population marked by the expression of *Clusterin* (*Clu*), which we termed “revival” stem cells (revSCs), that are critical for gut regeneration following irradiation and dextrate sulfate sodium-induced colitis (Ayyaz et al., 2019).

The intestinal epithelium is also critical for host defense against diverse species of parasitic helminths (Coakley and Harris, 2020). By executing the “weep-and-sweep” response, the epithelium increases mucus secretion and cell turnover to actively promote worm expulsion (Anthony et al., 2007; Cliffe et al., 2005; Shea-donohue et al., 2001). The type 2 immune response, orchestrated by IL-4 and IL-13, is fundamental to driving these epithelial responses during helminth infection. For example, IL-4 and IL-13 drive the differentiation and effector functions of secretory epithelial cells such as tuft and goblet cells

¹Department of Microbiology and Immunology, Meakins-Christie Laboratories, Research Institute of McGill University Health Centre, Montreal, Quebec, Canada;

²Department of Pathology, McGill University and Cancer Research Program, Research Institute of McGill University Health Centre, Montreal, Quebec, Canada; ³Division of Systems Biology, Montreal Clinical Research Institute, Montreal, QC, Canada; ⁴Department of Biochemistry and Molecular Medicine, University of Montreal, Montreal, Quebec, Canada; ⁵Department of Immunology, University of Washington, Seattle, WA; ⁶McGill University Health Centre, Meakins-Christie Laboratories, Department of Medicine, Division of Quantitative Life Sciences, Montreal, Quebec, Canada; ⁷Department of Human Genetics, Allen Edwards Centre for Pain Research, McGill University, Montreal, Quebec, Canada; ⁸McGill Interdisciplinary Initiative in Infection and Immunity, Montreal, Quebec, Canada; ⁹McGill Regenerative Medicine Network, Montreal, Quebec, Canada.

Correspondence to Irah L. King: irah.king@mcgill.ca; Alex Gregorieff: alex.gregorieff@mcgill.ca.

© 2022 Karo-Atar et al. This article is distributed under the terms of an Attribution–Noncommercial–Share Alike–No Mirror Sites license for the first six months after the publication date (see <http://www.rupress.org/terms/>). After six months it is available under a Creative Commons License (Attribution–Noncommercial–Share Alike 4.0 International license, as described at <https://creativecommons.org/licenses/by-nc-sa/4.0/>).

that produce lipid mediators (McGinty et al., 2020) and anti-helminth effector molecules (e.g., Relm β), respectively, that can promote worm expulsion (Barner et al., 1998; Horsnell et al., 2007; Herbert et al., 2009). However, early work showed that artificially enhancing the type 2 immune response by administration of long-acting IL-4 complexes was required to expel *Heligmosomoides polygyrus bakeri* (*Hpb*), a natural parasitic roundworm of mice, during primary infection (Urban et al., 1995). These results suggested that *Hpb* actively limits type 2 immunity.

While the ability of helminths to counter the host immune response during infection has been previously demonstrated, these effects have been largely attributed to modulation of the innate and adaptive immune compartments. Only recently have studies investigated whether helminths directly target the intestinal epithelium to regulate host defense (Drurey et al., 2021; Duque-Correa et al., 2020). By interrogating *Hpb* infection in mice, we demonstrate that these parasites directly reprogram the ISC compartment, independently of host-derived factors. This reprogramming event coincides with adult parasite colonization of the intestinal lumen and is characterized by activation of a fetal-like, regenerative Hippo pathway signature and the emergence of *Clu*-expressing revSCs. Morphological and single-cell transcriptomic analyses of intestinal organoids exposed to *Hpb*-conditioned medium (*Hpb*-CM) revealed direct targeting of the ISC compartment. *Hpb*-CM also suppressed IL-13-induced secretory cell differentiation, while deletion of type 2 cytokine signaling in vivo led to an epithelial-intrinsic expansion of revSCs and improved parasite fitness. Collectively, our study reveals how a helminth parasite co-opts a tissue development program to counter type 2 immune-mediated expulsion and maintain chronic infection.

Results and discussion

Enhanced fetal reprogramming of the intestinal epithelium at the luminal stage of *Hpb* infection

A recent report demonstrated that expression of *Ly6a* (encoding Sca-1) marks epithelial cells undergoing a fetal-like reversion event in granuloma-associated crypts during the tissue-dwelling stage of *Hpb* infection (6 d post-infection [dpi]; Nusse et al., 2018). We performed a kinetic analysis of duodenal tissue from *Hpb*-infected adult C57BL/6 mice using RNA sequencing (RNA-seq) that confirmed an increase in several fetal-associated genes (Mustata et al., 2013) including *Ly6a* expression on day 6 after infection (Fig. 1 A). However, we detected a more robust fetal gene signature during the luminal stage of infection (day 14), a time when adult worms establish residence alongside the intestinal villi (Fig. 1 A and B). To corroborate these results, we extracted intestinal crypts from *Hpb*-infected mice at different time points and cultured them under standard organoid growth conditions (Fig. 1 C). Adult intestinal organoids normally develop into polarized structures that mimic the crypt/villus architecture and are driven by abundant Lgr5⁺ ISCs (Date and Sato, 2015). Although crypts extracted at early time points after infection yielded typical budding organoids with abundant Paneth cells (Fig. 1 D), crypts on day 14 after infection developed into

hollow spheres resembling fetal organoids (Fig. 1, D and E; Mustata et al., 2013). Furthermore, crypts and epithelial cells isolated on day 14 after infection showed elevated expression of several fetal genes including *Clu*, *Il1rn*, and *Msln* (Figs. 1 F and S1 A). These findings were confirmed using single-molecule RNA in situ hybridization (RNAscope), which showed the loss of *Olfm4*⁺ ISC and a transient induction of *Ly6a* in granuloma-associated crypts on day 6, but sustained induction of *Il1rn* and *Il33* in distinct domains along the crypt-villus axis and the luminal stage-specific induction of *Clu* (Fig. 1, G and H; and Fig. S1 B).

Direct reprogramming of the ISC compartment by *Hpb*-CM

One interpretation of our findings is that luminal adult worms trigger fetal reprogramming because of the host immune response to parasite-induced breaches in the epithelium, as previously suggested for the larval stages of infection (Nusse et al., 2018). An alternative, but not mutually exclusive, possibility is that fetal reprogramming is driven by recognition of helminth-derived products by intestinal epithelial cells without a priori damage. To test the latter possibility, we stimulated organoids from the duodenum of uninfected mice with *Hpb*-CM collected from adult *Hpb* parasites. Strikingly, *Hpb*-CM-stimulated organoids assumed a spheroid morphology with robust induction of *Clu* and other fetal markers, while also downregulating the homeostatic ISC markers *Lgr5* and *Olfm4* (Fig. 2, A–D). RNA-seq followed by fast gene set enrichment analysis (fgSEA) confirmed the direct fetal-like reprogramming of organoids by *Hpb*-CM (Fig. 2, E and F; Mustata et al., 2013). Further analysis revealed that this reprogramming event was accompanied by the suppression of diverse lineages of differentiated epithelial cells (Fig. 2 G; and Fig. S1, C and D; Haber et al., 2017) including goblet and Paneth cells, similar to findings reported by Drurey et al. (2021). We also excluded the possibility that this fetal-like reversion of the epithelium is mediated by endotoxin contamination of *Hpb*-CM (Fig. S1, E–G), in agreement with previous studies establishing the inability of small intestinal organoids to respond to LPS due to lack of TLR4 expression (Kayisoglu et al., 2021). Importantly, helminth-induced fetal-like reprogramming of organoids was not observed in response to excretory-secretory products prepared from *Nippostrongylus brasiliensis* (*Nippo*-CM), a rat parasite that briefly transits through the small intestine (SI) of infected mice (Fig. 2, H–J). Collectively, these results suggest that fetal reprogramming is associated with parasites that chronically infect the SI.

The addition of EGF, Noggin, and R-spondin-1 (ENR) is an integral part of the organoid culture medium, reflecting the importance of morphogens such as WNTs and bone morphogenetic proteins in the regulation of ISC self-renewal and lineage commitment (Santos et al., 2018). To assess whether organoids depend on niche factors for helminth-driven reprogramming, established organoids were replated in the absence of ENR supplementation and stimulated with *Hpb*-CM. While the removal of niche factors resulted in an expected decrease in proliferation and loss of *Lgr5* expression, *Hpb*-CM was unable to initiate a fetal transcriptional response (Fig. 2, K–N), indicating

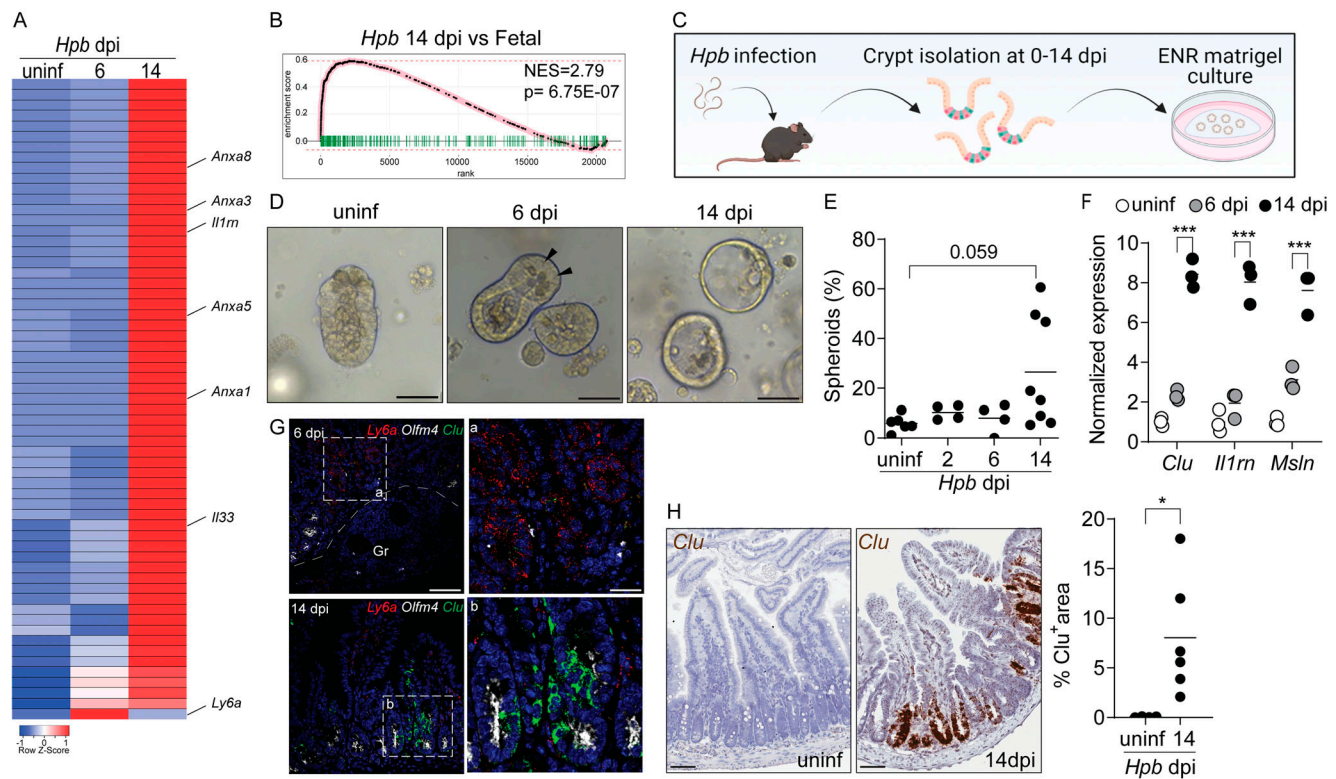


Figure 1. A fetal-associated transcriptional signature at the luminal stage of *Hpb* infection. (A) Analysis of RNA-seq dataset (Gentile et al., 2020) showing reads per kilobase million of fetal-associated genes (Mustata et al., 2013) in duodenal tissue 6 and 14 dpi. Specific genes of interest are depicted by name. Heatmap was created using the Heatmapper web tool (Babicki et al., 2016); uninf, uninfected. (B) GSEA of fetal-associated transcripts 14 dpi (in comparison to Mustata et al., 2013). NES, normalized enrichment score. (C–E) C57BL/6 mice were infected with 150 L3 *Hpb* larvae, and SI crypts were extracted 2, 6, and 14 dpi and plated in Matrigel domes for 24–48 h. Image in C created with Biorender.com. (D) Representative photomicrographs of organoids cultured from *Hpb*-infected intestines, 24 h after culture time point; arrowheads indicate Paneth cells. (E) Frequency of organoids with spheroid morphology. (F) qPCR analysis of organoids cultured from *Hpb*-infected intestines. (G) RNAscope of fetal-associated transcripts in *Hpb*-infected tissue. a and b are enlarged insets from left panels; Gr, granuloma. (H) Colorimetric RNAscope of *Clu* mRNA and quantification of *Clu*⁺ areas. Scale bar, 50 μ m (D–G); 100 μ m (H). Data shown are representative of one (A and B) or two or more (D–H) independent experiments, $n > 3$ biological replicates. Statistical tests: nonparametric one-way ANOVA (E), t test (F and H); *, $P < 0.05$; ***, $P < 0.005$.

that reprogramming requires niche factors and likely targets a mitotic progenitor cell.

***Hpb*-CM reprogramming of the ISC compartment is partially dependent on the Hippo signaling pathway**

The Hippo signaling pathway is a well-established regulator of tissue regeneration in response to damage and linked to fetal reprogramming (Yui et al., 2018; Gregorieff and Wrana, 2017). Consistently, *Hpb* infection induced nuclear translocation of YAP, a transcriptional effector of Hippo signaling, in the intestinal epithelium at the luminal stage of infection (Fig. S2 A). Although many of the fetal-associated genes, including *Clu*, are YAP target genes, *Hpb*-CM-induced fetal-like reprogramming of organoids and in vivo *Clu* induction were only partially Yap dependent (Fig. S2, B–D; and data not shown). Furthermore, treatment of organoids with recombinant CLU was not sufficient to induce spheroids, and stimulation of *Clu*-deficient organoids with *Hpb*-CM did not prevent organoid reprogramming (Fig. S2, E–G; and not depicted). Finally, animals lacking YAP in the intestinal epithelium (Villin^{Cre}Yap^{fl/fl} mice) had worm burdens equivalent to those of littermate controls, indicating that this

transcriptional activator is dispensable for *Hpb* persistence (Fig. S2 H). Thus, *Clu* expression represents a broader transcriptional network mediating fetal-like reprogramming that does not exclusively rely on YAP-dependent signaling.

***Hpb*-CM-induced epithelial reprogramming is not regulated by IFN γ signals**

A previous study demonstrated that the induction of *Ly6a*⁺ ISCs in granuloma-associated crypts was IFN γ dependent (Nusse et al., 2018). Although our RNA-seq and RNAscope data (Fig. 1, A and G) confirmed the induction of *Ly6a* mRNA on day 6 after *Hpb* infection, expression of this gene was decreased by day 14 after infection. Nevertheless, we tested the possibility that the fetal reversion induced by *Hpb*-CM is regulated by IFN γ . As expected for an IFN γ -inducible gene (Khan et al., 1990), *Ly6a* was induced following organoid stimulation with IFN γ . However, IFN γ did not induce other fetal-associated genes we tested, and its addition to *Hpb*-CM-stimulated organoids had no effect or decreased induction of other fetal genes (Fig. S2, I–L). Therefore, IFN γ signals do not support *Hpb*-CM-induced epithelial reprogramming.

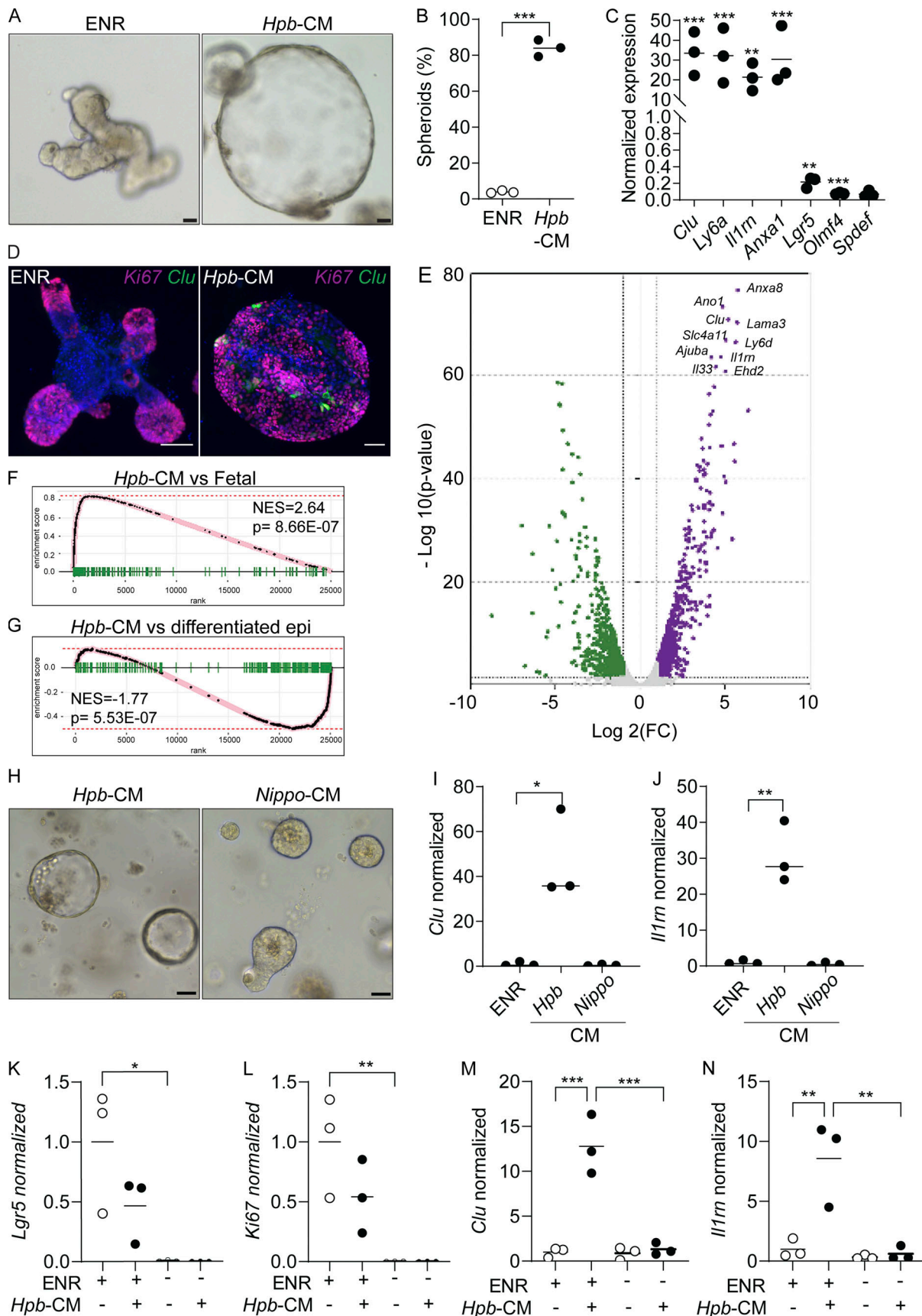


Figure 2. ***Hpb-CM* directly induces fetal reversion of intestinal organoids.** (A) SI organoids were stimulated with ENR (control) or *Hpb-CM* medium for 24 h after 3 d in culture. (B) Frequency of organoids with a spheroid morphology. (C) qPCR analysis of SI organoids stimulated with *Hpb-CM* for 24 h from the plating

of fresh crypts. **(D)** Confocal photomicrographs of SI organoids from *Clu*^{GFP} crypts (Ayyaz et al., 2019) stimulated with *Hpb*-CM for 24 h on day 3 of culture. **(E)** Volcano plot of differentially expressed genes from RNA-seq analysis comparing *Hpb*-CM-treated organoids to control organoids, false discovery rate < 0.05. For a complete list of differentially expressed genes, see Table S1. **(F and G)** GSEA of fetal-associated transcripts (F) and differentiated epithelial cell markers (G). NES, normalized enrichment score. **(H–J)** Representative photomicrographs (H) and qPCR analysis (I and J) of SI organoids stimulated with *Nippo*-CM for 24 h. **(K–N)** qPCR analysis of SI established organoids stimulated with *Hpb*-CM for 24 h in the presence or absence of ENR. Scale bar, 50 μ m. Data shown are representative of two or more independent experiments, $n = 3$ biological replicates; statistical tests: t test (B, C, I, and J), two-way ANOVA (K–N); *, $P < 0.05$; **, $P < 0.01$; ***, $P < 0.005$.

Emergence of revSCs at the luminal stage of *Hpb* infection

For a more in-depth analysis into the effect *Hpb*-CM exerts on the ISC compartment, we performed single-cell RNA-seq (scRNA-seq) on control and *Hpb*-CM-stimulated organoids. Clustering of cells was performed using previously published epithelial lineage-defining markers (Haber et al., 2017; Ayyaz et al., 2019). Our analysis yielded eight cell clusters, identifying stem (*Lgr5*⁺ crypt base columnar cells [CBCs]) and progenitor cells as well as mature secretory populations (Fig. 3, A and B). In accordance with our bulk RNA-seq results (Fig. 2), *Hpb*-CM expanded a distinct cell cluster enriched in fetal genes, which was rare in control-treated organoids, that we previously identified as revSCs following irradiation (Ayyaz et al., 2019). By contrast, goblet and Paneth cell clusters were significantly reduced in *Hpb*-CM-stimulated organoids, whereas secretory progenitor cells (marked by *Atoh1* and *Spdef* expression) were enriched (Fig. 3, A and C). Under these culture conditions, we were not able to detect a sufficient number of tuft cells for statistical analysis. Next, we performed trajectory analyses in which the pseudotime scale indicates gene expression changes that inform the potential differentiation paths from a chosen source population (i.e., CBCs). This analysis demonstrated that transit amplifying (TA) cells are displaced within the Uniform Manifold Approximation and Projection (UMAP) space by revSC expansion in *Hpb*-CM-stimulated organoids (Figs. 3 D and S2 M), implying a central role for revSCs in driving renewal of the gut epithelium during *Hpb* infection in vivo. To validate this possibility, we performed lineage-tracing studies using tamoxifen-inducible *Clu* fate-mapping mice (Ayyaz et al., 2019). As shown in Fig. 3, E–G, labeling *Clu*-expressing cells on day 5–7 after infection and assessing the tissue 12 d later yielded rare Tomato (Tom)⁺ cells. By contrast, labeling *Clu*-expressing cells on day 12 after infection resulted in robust generation of Tom⁺ ribbons along the crypt-villus axis 12 d later, a pattern indicative of progeny derived from *Clu*-expressing stem cells. Consistent with their stem cell capacity, revSCs gave rise to Tom⁺ cells that also expressed DCLK or UEA1, representing tuft and goblet cells, respectively. Remarkably, however, these secretory lineages were less abundant in Tom⁺ ribbons compared with Tom[−] ribbons (Fig. 3, H and I). Together, these data suggest that *Hpb* profoundly rewires the differentiation trajectories of ISCs and TA cells in favor of revSCs, which in turn, display a reduced capacity to generate secretory cell lineages with direct anti-helminth activity.

An oxidative stress response mediates *Hpb*-induced fetal reversion of intestinal organoids

To gain mechanistic insight into how *Hpb*-CM reprograms the ISC compartment, we next assessed the transcriptional changes

within each cluster identified in our scRNA-seq experiment. The number of differentially expressed genes (DEGs) was highest in enterocytes and TA cells following *Hpb*-CM stimulation, and the most significant pathways identified were seen in the TA cell compartment (Fig. 4, A and B). Specifically, pathway analysis indicated a metabolic change in organoids following *Hpb*-CM stimulation as well as a striking oxidative stress response (Fig. 4 B). To exclude the possibility that nutrient deprivation was contributing to fetal reprogramming, we used purified HES (Valanparambil et al., 2014). To this end, *Hpb*-CM was concentrated over a 3-kD filter and used to stimulate organoids at a 10-fold dilution. As shown in Fig. 4, C–E, diluting concentrated HES in fresh ENR resulted in induction of spheroid formation as well as the fetal-associated genes *Clu* and *Ilrn* to the same extent as *Hpb*-CM, indicating that nutrient deprivation is not likely the cause of cell reprogramming. In additional agreement with the induction of an oxidative stress response, *Hmox1*, a well-known indicator of oxidative stress (Poss and Tonegawa, 1997), was induced following *Hpb*-CM stimulation (Fig. 4 F). We next directly tested the role of oxidative stress by stimulating organoids with *Hpb*-CM in the presence of elevated concentrations of the antioxidant *N*-acetylcysteine (NAC; Ezeriņa et al., 2018). The addition of NAC suppressed spheroid formation and the induction of fetal-associated genes (Fig. 4, G–J), establishing the oxidative stress response as an important mediator of *Hpb*-driven fetal-like reversion of the ISC compartment.

Counter-regulation of the ISC compartment by *Hpb* and type 2 cytokines

Tuft and goblet cells are secretory epithelial lineages that orchestrate the initiation and effector functions, respectively, of the type 2 immune response that is responsible for parasitic helminth expulsion (Coakley and Harris, 2020; von Moltke et al., 2016; Gerbe et al., 2016). Therefore, building on our scRNA-seq and imaging results (Fig. 3), we tested whether *Hpb*-CM was able to directly inhibit type 2 cytokine-induced differentiation of secretory cells. While IL-13 stimulation of organoids resulted in robust *Spdef*, *Clca1* (encoding Gob5), *Muc2*, and *Dclki* mRNA expression, the addition of *Hpb*-CM prevented induction of these lineage-specific transcripts (Fig. 5, A–D; Drurey et al., 2021). Suppression of IL-13-induced differentiation of tuft and goblet cells was also confirmed by immunofluorescence microscopy (Fig. 5, E–G). By contrast, pretreatment of organoids with IL-13 to promote secretory cell differentiation limited fetal gene expression upon subsequent exposure to *Hpb*-CM (Fig. 5, H and I). Therefore, *Hpb*-CM and type 2 cytokines act in a counter-regulatory manner on the ISC compartment.

The main driver of secretory cell differentiation is STAT6-dependent type 2 cytokine signaling (via IL-4 and IL-13;

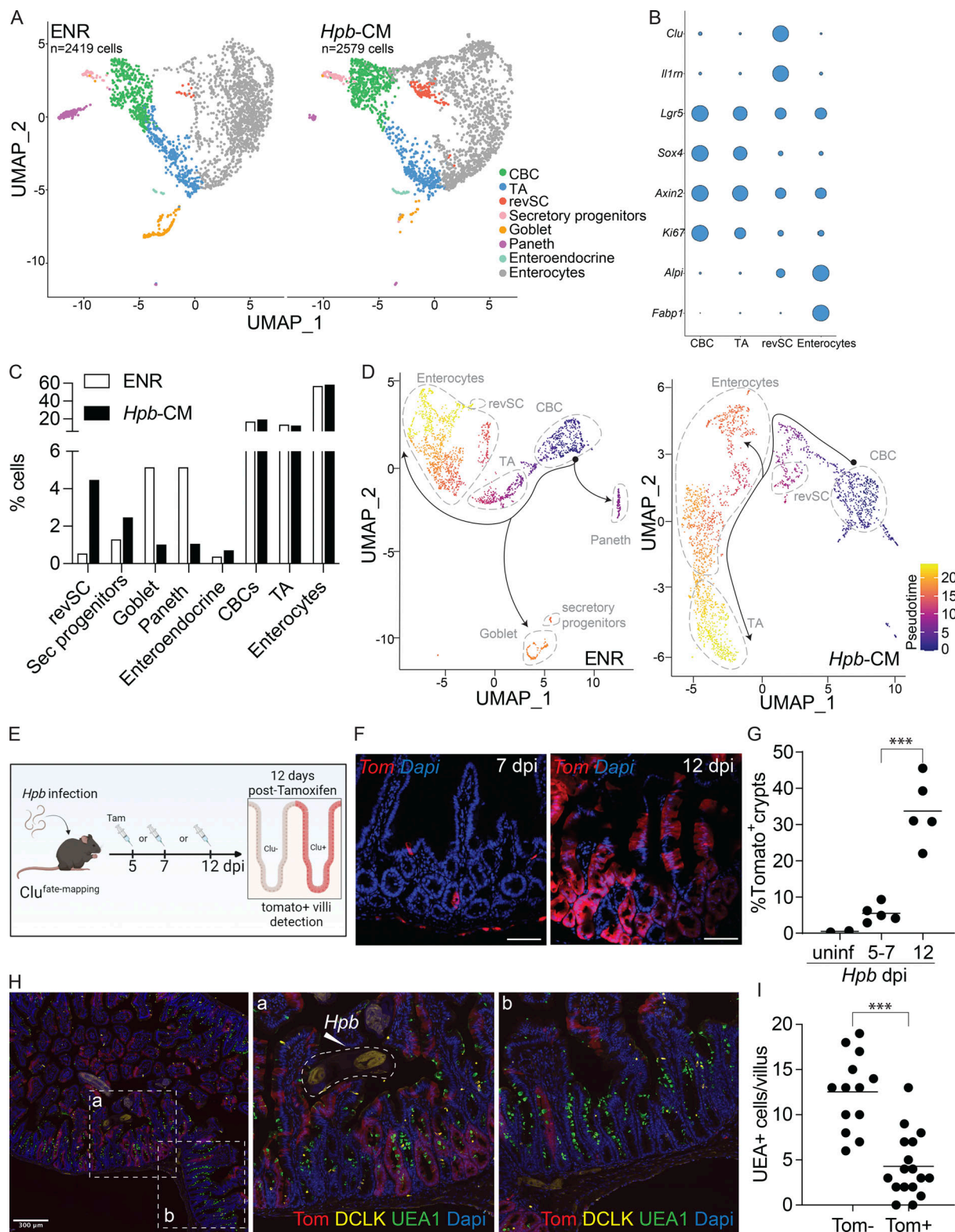


Figure 3. *Hpb-CM* expands revSCs and limits secretory cell differentiation. SI organoids were stimulated with *Hpb-CM* for 24 h from the plating of fresh crypts, and scRNA-seq analysis was performed. **(A)** UMAP projection plots; colors represent cells clustered together based on gene expression similarity. **(B)** Representative cluster identifying markers; circle size represents average expression of indicated transcripts (complete gene expression list can be found in Table S2). **(C)** The proportion of each cluster within each sample is presented. **(D)** Trajectory analysis using CBCs as the pseudotime source variable (pseudotime = 0). **(E–G)** *Clu* fate-mapping (*Clu*-CreERT; Rosa26-LSL-tdTomato; Ayyaz et al., 2019) mice were infected with *Hpb*, and *Clu*⁺ Tom⁺ cells were labeled by tamoxifen injection 5, 7, or 12 dpi and imaged 12 d after each injection; scale bar, 100 μ m; image created with Biorender.com. **(H and I)** Immunofluorescent staining for DCLK (yellow), UEA1 (green), and DAPI (blue) as well as detection of Tom (red) in *Clu* fate-mapping mice on 24 dpi (mice were injected with tamoxifen on 12 dpi). Data shown are representative of one (A–D) or three or more (E–I) independent experiments, $n = 3$ –5 biological replicates. Statistical tests: two-way ANOVA (G), t test (I); ***, $P < 0.005$.

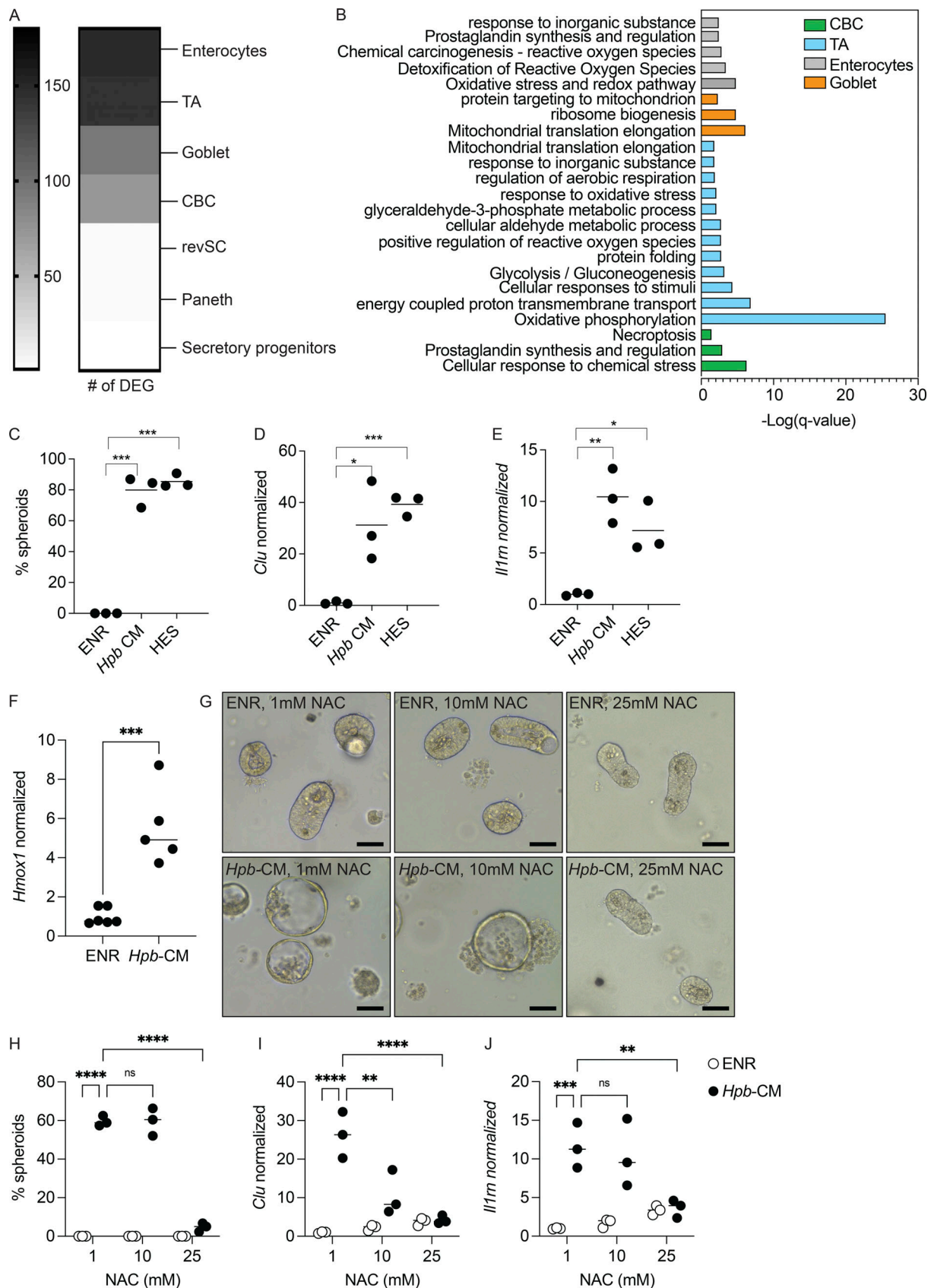


Figure 4. **An oxidative stress response drives Hpb-CM-induced fetal reversion of intestinal organoids.** (A) Number of DEGs in each cell cluster identified by scRNA-seq analysis described in Fig. 3. (B) Pathway analysis based on DEGs was performed using Metascape (Zhou et al., 2019). (C–E) SI organoids were stimulated at the start of culture with ENR (control), Hpb-CM, or a 10-fold dilution of HES for 24 h. (C) Frequency of organoids with a spheroid morphology.

(D and E) qPCR analysis of the indicated genes normalized to *Hprt* expression. (F–J) SI organoids were stimulated at the start of culture with ENR (control) or *Hpb*-CM. qPCR analysis is shown (G–J). SI organoids were stimulated with ENR (control) or *Hpb*-CM in the presence of increasing concentrations of NAC for 24 h. qPCR analysis of the indicated genes is shown. Scale bar, 50 μ m; data shown are representative of one (A and B) or three or more (C–H) independent experiments, $n = 3$ –5 biological replicates. Statistical tests: one-way ANOVA (C–E), t test (F), two-way ANOVA (H–J); *, $P < 0.05$; **, $P < 0.01$; ***, $P < 0.005$; ****, $P < 0.001$.

Finkelman et al., 2004). To test the involvement of type 2 immune signaling in the regulation of *Hpb*-induced fetal-like reprogramming in vivo, we infected *Stat6*-deficient mice with *Hpb*. Remarkably, loss of STAT6 resulted in increased ex vivo fetal-associated spheroid formation and in situ intestinal *Clu* expression (Fig. 5, J–M). To specifically test the role of epithelial-intrinsic type 2 immune signaling in the induction of *Clu*⁺ revSCs, *Villin*^{Cre}*Il4ra*^{fl/fl} mice (*Il4ra*^{ΔIEC}) were infected with *Hpb*, and a trend toward increased in situ *Clu* expression was detected (Figs. 5 N and S3 A). We next assessed *Hpb* fitness and persistence by evaluating adult worm burden in *Stat6*^{−/−} mice (Fig. S3 C) and fecal egg counts in *Stat6*^{−/−} and *Il4ra*^{ΔIEC} mice (Fig. 5, O and P). In association with enhanced *Clu* expression, *Stat6*^{−/−} and *Il4ra*^{ΔIEC} mice had elevated worm and egg burdens on day 14 after infection, suggesting that epithelial-intrinsic type 2 immune signaling is needed to limit the induction of revSCs and worm persistence. To control for differences in parasite fitness, we took a gain-of-function approach and treated *Clu*-fate mapping mice with low-dose IL-4 complexes (IL4C) on days 10, 12, and 14 after *Hpb* infection. This transient amplification of type 2 cytokine signals led to a reduction of *Hpb*-induced Tom⁺ ribbons without a difference in *Hpb* egg production (Fig. 5 Q and Fig. S3, B and D). Finally, to assess the immune landscape in *Stat6*^{−/−} and *Il4ra*^{ΔIEC} mice following *Hpb* infection, we performed immunophenotyping of the SI, Peyer's patches (PPs), and mesenteric lymph nodes (MLNs) by flow cytometry (Fig. S3, E–J). As expected, accumulation of GATA3⁺ Th2 cells in the MLNs, PPs, and SI of *Hpb*-infected animals was largely eliminated in *Stat6*^{−/−} mice. By contrast, infected *Il4ra*^{ΔIEC} mice showed numbers of Th2 cells similar to littermate controls, indicating that direct type 2 cytokine signaling, not immune deviation per se, is responsible for driving epithelial reprogramming. Taken together, our data establish a balanced regulation of the ISC compartment by helminths and type 2 immune signaling that supports durable infection.

Expulsion of multicellular helminths from the intestinal lumen requires production of type 2 cytokines that direct the epithelial weep-and-sweep response (Anthony et al., 2007). It is well documented that helminths secrete immunomodulatory factors that target type 2 cytokine-producing cells to limit anti-helminth immunity (Hewitson et al., 2009). Here we demonstrate that helminths also evade expulsion through direct reprogramming of the intestinal epithelium into a fetal-like state. Interestingly, similar to our findings using adult *Hpb*-CM, Drurey et al. (2021) showed that *Hpb* infective L3 larvae were also capable of suppressing IL-4/IL-13-induced differentiation of goblet and tuft cells. However, they did not test the ability of L3 larvae to induce fetal-like reversion of the epithelium, an event we found to be dominant during the luminal stage of infection.

This result raises the possibility that helminth-induced fetal reversion and inhibition of secretory cell formation might be two mutually exclusive events, an avenue of great interest for future studies.

Taken together, our results suggest that, although fetal reversion of the intestine is critical for regeneration upon injury, parasites such as *Hpb* that have evolved with their hosts coopt this restorative pathway to persist and continue their life cycle. Our study provides a new conceptual framework that not only may lead to improved anthelmintics that interfere with parasite-epithelium signaling networks, but also spur helminth-based therapies to rejuvenate the intestinal barrier following acute injury.

Materials and methods

Animals

All experiments were performed in accordance with the McGill University Health Centre Research Institute Animal Resource Division with approved animal use protocol #7977. WT C57BL/6, *Stat6*^{−/−}, and *Yap*^{flxed} mice were obtained from The Jackson Laboratory. *Villin*^{Cre} mice were kindly provided by Nicole Beauchemin (McGill University). *Il4ra*^{fl/fl} mice were kindly provided by Frank Brombacher (International Center for Genetic Engineering and Biotechnology, Cape Town, South Africa). *Villin*^{Cre}*Il4ra*^{fl/fl} and *Villin*^{Cre}*Yap*^{fl/fl} were bred in-house. *Clu*-CreERT2; Rosa26-LSL-tdTomato, *Clu*^{GFP}, and *Clu*^{CreERT2/creERT2} were generated as previously described (Ayyaz et al., 2019). Homozygote *Clu*-CreERT2 are effectively *Clu* deficient (*Clu*^{−/−}; Ayyaz et al., 2019). All mice were bred and maintained under specific pathogen-free conditions. All experiments were performed using littermates with the exception of *Stat6*^{−/−} mice. Female and male mice 6–10 wk of age were used.

Helminth infection

For *Hpb* infection, mice were infected by gavage with 150 L3 stage larvae diluted in sterile water. Mice were euthanized at the indicated time points, and tissues were harvested for analysis. For histology, the proximal 5 cm of the SI was harvested on the indicated days, flushed, and fixed in 10% formalin for 24 h before standard formalin-fixed, paraffin-embedded (FFPE) processing. For *Nippo* infection, infectious third-stage larvae (L3) were maintained by passaging through Lewis rats (Envigo), as previously described (Liang et al., 2012). For histology of *Nippo*-infected intestines, mice were infected s.c. with 500 L3 larvae. The proximal 10–12 cm of the SI was harvested after 7 d, flushed, and fixed in 10% formalin for 2 h. Intestines were then rolled into “Swiss rolls,” placed in a tissue cassette, and fixed for an additional 18–24 h before standard FFPE processing.

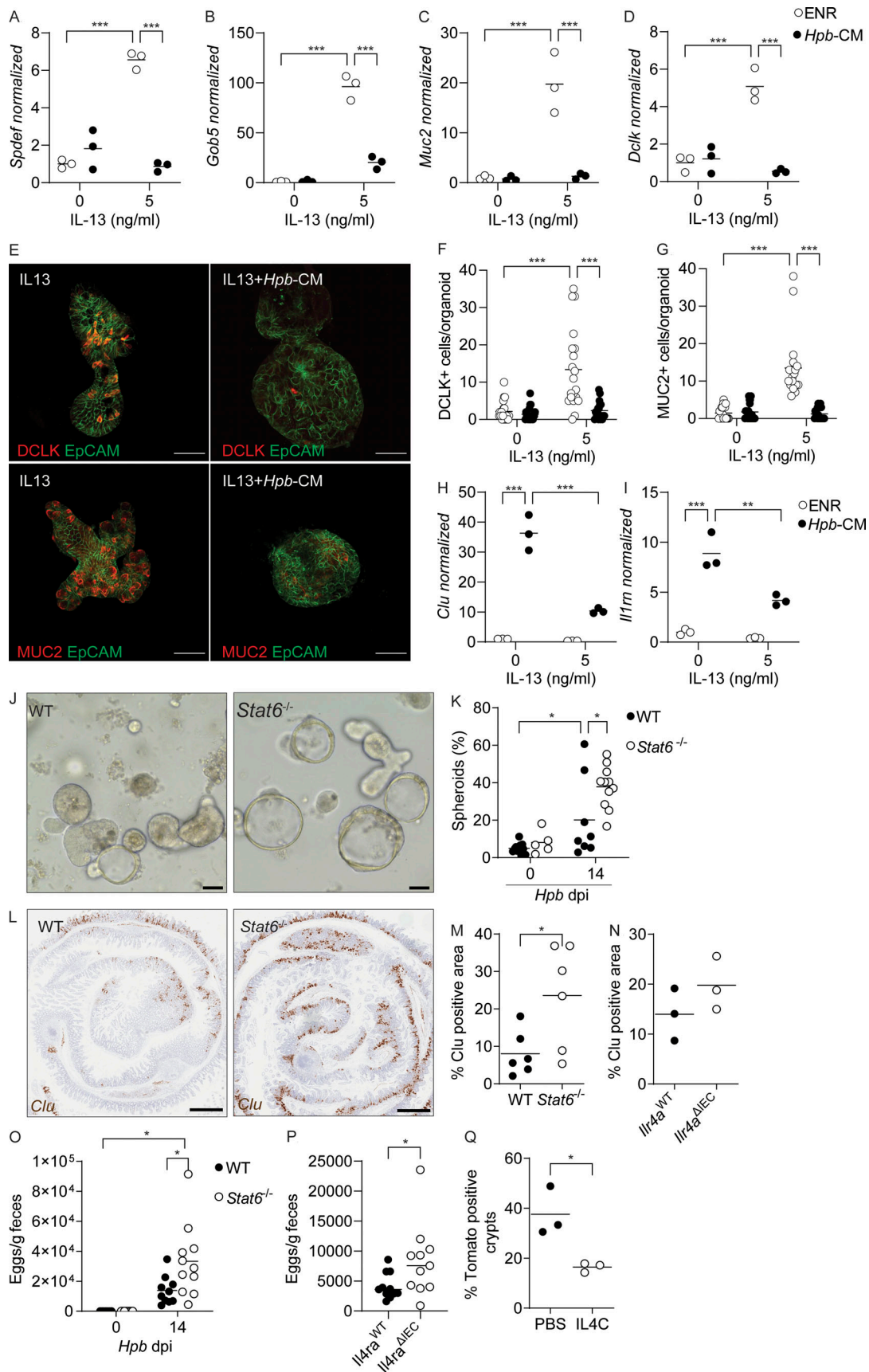


Figure 5. **Counter-regulation of the ISC compartment by helminths and type 2 cytokine signaling.** (A–D) SI organoids were stimulated at the start of culture with *Hpb*-CM ± IL-13, and qPCR analysis was performed for the indicated genes 48 h later. (E) Photomicrographs of organoids stimulated with *Hpb*-CM

± IL-13 for 48 h. **(F and G)** DCLK⁺ (F) and MUC2⁺ (G) cells were counted in 20 individual organoids from two mice. **(H and I)** SI organoids were stimulated with IL-13 for 10 d (over three passages) before *Hpb*-CM stimulation, and qPCR analysis for the indicated genes was performed 24 h after *Hpb*-CM stimulation. **(J and K)** C57BL/6 and *Stat6*^{-/-} mice were infected with *Hpb*, and crypts were extracted 14 dpi and plated in Matrigel domes for 24 h. Representative photomicrographs (J) and quantification of ex vivo spheroid generation (K) are shown. **(L and M)** *Clu* expression by in situ hybridization of WT and *Stat6*^{-/-} tissues 14 dpi. Representative photomicrographs (L) and quantification (M) of *Clu*⁺ tissue area. **(N)** Quantification of *Clu*⁺ intestinal tissue from *Il4ra*^{WT} and *Il4ra*^{ΔIEC} mice 14 dpi. **(O and P)** Fecal *Hpb* egg counts from WT and *Stat6*^{-/-} (O) and *Il4ra*^{WT} and *Il4ra*^{ΔIEC} (P) mice 14 dpi. **(Q)** Quantification of *Clu*⁺ intestinal area from *Clu* fate-mapping mice injected with tamoxifen 12 dpi and PBS or IL-4C 10, 12, and 14 dpi. Tissues were harvested on day 24 after infection. Scale bar, 50 μm (E and J); 1 mm (L). All data shown are representative of two or more independent experiments, *n* > 3 biological replicates. Statistical tests: two-way ANOVA (A–K and O), *t* test (M, N, and Q); *, *P* < 0.05; **, *P* < 0.01; ***, *P* < 0.005.

SI organoid culture

The SI was harvested, flushed with PBS, cut into three 10-cm pieces, and opened longitudinally. Intestine pieces were rinsed with PBS and then incubated in 2 mM EDTA at 4°C for 30 min with gentle agitation. Crypts were further released from the SI by vigorous shaking in 10 ml PBS, three times, and passed through a 70-μm cell strainer. Isolated crypts were resuspended in 10 ml basal organoid medium (Advanced DMEM/F12 [Gibco], 10 mM Hepes [Gibco], 1× GlutaMAX [Gibco], and 1% penicillin/streptomycin [Gibco]). Crypts were plated in 30 μl Matrigel (Corning) domes in 24-well plates, and 500 μl of culture medium was added to each well. Organoids culture medium (ENR): basal organoid medium with the addition of N2 Supplement (1:100; Gibco), B27 Supplement (1:50; Gibco), 1 mM NAC, 50 ng/ml recombinant EGF, in-house made R-spondin 1, and Noggin CM (1:50). Organoids were maintained for the indicated times and passaged every 3–4 d by physical dissociation of the Matrigel and replating in fresh ENR medium. For *Hpb*-CM and/or *Nippo*-CM stimulation, *Hpb*-CM and/or *Nippo*-CM were supplemented with N2 (1:100; Gibco), B27 (1:50; Gibco), 1 mM NAC, 50 ng/ml recombinant EGF, in-house made R-spondin 1, and Noggin CM (1:50). For IL-13 stimulation, organoids were treated with 5 ng/ml of IL-13 simultaneously with *Hpb*-CM for 24 h or pretreated with 5 ng/ml IL-13 for 10 d (over three passages) before stimulation with *Hpb*-CM for 18 h.

Conditioned medium and HES preparation

To generate *Hpb*-CM, WT mice were infected by gavage with 400 L3 *Hpb* larvae, and adult worms were manually harvested from the SI after 21 d as previously described (Moreno et al., 2011). Sterile adult worms were then cultured overnight in organoid basal medium at ~130 worms/ml. The following day, culture medium containing helminth secretory products was removed, filtered through a 0.2-μm filter, and kept at -80°C until use. For *Nippo*-CM preparation, rats were infected s.c. with 3000 L3 *Nippo*, and adult worms were manually harvested from the SI after 7 d and cultured as described for *Hpb*-CM. For HES preparation, *Hpb*-CM was concentrated using a 3-kD Amicon filter tube and used at 10-fold dilution in fresh ENR medium.

ENR withdrawal

SI organoids were grown in ENR-supplemented medium. After 10 d of culture, organoids were passaged and replated in the presence or absence of growth factors for 24 h before stimulation with *Hpb*-CM for an additional 18 h.

Organoid whole-mounting and confocal microscopy

Established organoids were passaged and replated in a 1:1 ENR: Matrigel solution; 30-μl domes were plated on Nunc Lab-Tek II Chamber Slides and incubated overnight in 200 μl medium at 37°C. Organoids were then treated with 5 ng/ml of IL-13 in ENR or simultaneously with *Hpb*-CM for 48 h. After stimulation, domes were fixed in 10% formalin for 30 min at room temperature (RT), and permeabilized with PBS-T (PBS + Triton 0.5%) for 15 min. The samples were blocked with 200 μl blocking solution (3% BSA in PBS) for 1 h at RT. Organoids were incubated with primary antibodies overnight at 4°C, followed by incubation with secondary antibodies at RT for 1 h. The nuclei were stained with DAPI (1 μg/ml). Specific antibodies include anti-mouse/rat Ki67 eFluor 660 (Invitrogen), anti-mouse CD326 (EpCAM) Alexa Fluor 488 (BioLegend), goat anti-GFP (Invitrogen), anti-goat IgG Alexa Fluor 555 (Invitrogen), rabbit anti-mouse Dclk (Abcam), rabbit anti-mouse Muc2 (Abcam), and goat anti-rabbit IgG Alex Fluor 555. All fluorescent images were taken on a Zeiss Confocal LSM700, using a 20×/0.8 M27 Plan-Apochromat objective, after mounting with Invitrogen Prolong Glass Antifade Mounting solution. Tile scanning (5 × 5 tiles) was performed as well as Z-stacking to generate images analyzed using Fiji software (Schindelin et al., 2012).

RNAscope

RNAscope was performed according to manufacturer instructions (ACD Bio). RNAscope probes: *Clu* (cat# 427891); *Il1rn* (cat# 495101); *Il33* (cat# 400591-C2); and *Ly6a* (cat# 427571-C2). Images were taken on a Leica Aperio AT Turbo digital pathology scanner, using a 20×/0.75 Plan Apo objective, after mounting with Cytoseal 60 (Thermo Fisher Scientific). Quantification of *Clu* expression by colorimetric RNAscope was performed after 20× magnification scanning of entire 5-cm tissue rolls, using the pixel count function of Qupath, a digital pathology image analysis software (Bankhead et al., 2017).

RNA extraction and quantitative PCR (qPCR)

RNA was extracted using Tri reagent (Sigma-Aldrich) or Pure-Link RNA Mini kit (Invitrogen) according to manufacturer instructions. Primers used: *Clu* forward, 5'-AAACCAACGCAGAGC GCAAG-3', and reverse, 5'-CTCCAGAGCATCCTCTTTCTTCTT-3'; *Il1rn* forward, 5'-AGGCATGTGCTCTACCATCATGCT-3', and reverse, 5'-GCCGACATGGAATAAGGCTGGC-3'; *Msln* forward, 5'-TCTCCAAACAGTGGTGTGGG-3', and reverse, 5'-AAGCAGTAG GAAGCTTCGGC-3'; *Lgr5* forward, 5'-AGAGCCTGATACCATCTG CAAAC-3', and reverse, 5'-TGAAGGTGCTCCACACTGTTGC-3';

Olfm4 forward, 5'-GCTCCTGGAAGCTGTAGTCA-3', and reverse, 5'-GGCCCCAGGCACCATATTTA-3'; Gob5 forward, 5'-CATCGC CATAGACCACGACG-3', and reverse, 5'-TTCCAGCTCTCGGGA ATCAA-3'; Muc2 forward, 5'-CTGACCAAGAGCGAACACAA-3', and reverse, 5'-CATGACTGGAAGCAACTGGA-3'; Spdef forward, 5'-TCCTCTCTGCTCACTCTGAA-3', and reverse, 5'-AGAGCTCAT GTGTATCCCTAGA-3'; Dclk forward, 5'-AACGTCAAGACCACC TCAGC-3', and reverse, 5'-GAGCCGTCTTCTTGTTCAGC-3'; Il33 forward, 5'-GACACATTGAGCATCCAAGG-3', and reverse, 5'-TGATTGACTTGACAGGACAGG-3'; Ly6a forward, 5'-GGAGGCAGC AGTTATTGTGG-3', and reverse, 5'-GCTACATTGCAGAGGTCT TCC-3'; Anxal forward, 5'-CAACCATCGTGAAGTGTGCC-3', and reverse, 5'-ATGCCTTATGGCGAGTTCCG-3'; and Ki67 forward, 5'-CCTGGTCAACATCAAGCGG-3', and reverse, 5'-ATTCAATAC TCCTTCCAAACAGGC-3'.

Bulk RNA-seq

SI organoids were stimulated with ENR (control) or ENR + *Hpb*-CM medium for 24 h from the start of culture. RNA was extracted using Trizol reagent (Sigma-Aldrich), and quality was checked with the Bioanalyzer RNA 6000 kit. Libraries were prepared using the NEB mRNA stranded library prep Kit (New England Biolabs) and paired-end sequenced on the NovaSeq 6000 at 25 million reads per sample. RNA-seq reads were aligned to the mm10 reference genome using STAR (Dobin et al., 2013). Read counts were calculated using the strand-specific exonic reads of each gene, and duplicate genes were merged using HOMER (Heinz et al., 2010). Transcripts per million were used to evaluate the correlation among replicates for quality control. Differential gene expression was calculated from the raw read counts using edgeR (Robinson et al., 2009). Data sets presented in the manuscript can be found at GEO, accession no. GSE199227.

GSEA

For pathway analyses, custom gene sets were built using genes differentially (up- or down-regulated) expressed in previous cell type-specific transcriptomic studies. A fetal-associated gene list was built using Table S1 in Mustata et al. (2013). A differentiated epithelial cell marker list was built using Table S4 in Haber et al. (2017). Transcriptomes from this work were analyzed for enrichment in differentially expressed genes in those gene sets using the “fgsea” R package (<https://github.com/ctlab/fgsea>; Korotkevich et al., 2021).

scRNA-seq

SI organoids were stimulated with ENR (control) or ENR + *Hpb*-CM medium for 24 h on day 0 of culture. Single-cell suspensions were prepared by manual disturbance of Matrigel domes followed by incubation in TrypLE (Gibco) for 40 min at 37°C and loaded on a Next GEM Chip G (PN-1000120) together with Next GEM Single Cell 3' GEM Kit v3.1 (PN-1000121). Single cells were captured on a 10× Genomics Chromium controller with a recovery target of 5,000 cells per sample. cDNAs were generated following the 10X Genomics protocol. cDNAs were size selected using SPRIselect beads from Beckman Coulter (B23318), and their quality was checked with a Bioanalyzer High Sensitivity

DNA Kit from Agilent (5067-4626). One quarter of the total cDNA was used to generate libraries using Next GEM Single Cell Library Kit (PN-1000121) and barcoded using the Single Index Kit Set A (PN-111213) following the 10X protocol. Libraries were size-selected using SPRIselect beads, and their quality was checked with the Bioanalyzer High Sensitivity DNA Kit. Libraries' sizes were centered at 440 bp and paired-end sequenced on a NovaSeq 6000 at 125 M reads per sample. Single-cell matrices were generated using Cellranger (v4.0.0) provided by 10X Genomics. Sequences were aligned with the mm10 mouse transcriptome. Matrices were imported and analyzed with the R package “Seurat” (v4.0.3; Butler et al., 2018). We filtered out genes expressed in fewer than three cells and low-quality cells expressing <200 genes. Cells with >100,000 transcripts were removed, as they likely represent cell doublets (Butler et al., 2018). In addition, immune cells (marked by Cd3g) were removed from the analysis. Each matrix was normalized with Seurat's “NormalizeData” function using “LogNormalize” as the normalization method and a scale factor equal to 10,000 (default value). Matrices were integrated using the “IntegrateData” function. Linear dimensionality reduction was performed using the “RunPCA” function. Nonlinear dimensionality reduction was then performed using the “RunUMAP” function, considering the Euclidean distances of the first 30 PCA (principal component analysis) components. *k*-Nearest neighbors graph construction was performed using the “FindNeighbors” function, which also considered the first 30 PCA components. Clustering (Louvain method) was performed using the “FindClusters” function, with a resolution equal to 1.5. Differential expression analysis was performed using the “FindAllMarkers” function to detect markers considering positive log-transformed fold-change values >0.25. Finally, trajectory analysis was performed with the R package “Monocle3” (v0.2.3.0; Trapnell et al., 2014) using CBCs as the source of the pseudotime variable (pseudotime = 0). To display trajectory analysis results, UMAP was performed on each matrix using the “reduce_dimension” function found in the Monocle3 package (McInnes et al., 2018). Data sets presented in the manuscript can be found at GEO, accession no. GSE199227.

Metascape analysis

All differentially expressed genes, in a specific cluster, between ENR and *Hpb*-CM samples were used in the online Metascape tool (Zhou et al., 2019), and the default “express analysis” option was chosen.

Clu lineage-tracing studies

Tamoxifen-inducible *Clu* fate-mapping mice (*Clu*-CreERT/+; Rosa26-LSL-tdTomato; Ayyaz et al., 2019) were infected with 150 *Hpb* larvae. 2.5 mg tamoxifen (Sigma-Aldrich) was injected i.p. 5, 7, and 12 dpi. To allow the proliferation and differentiation of potential *Clu*⁺ stem cells, SIs were harvested 12 d after tamoxifen injection for histological analysis. Specifically, the proximal 5 cm of the duodenum was fixed overnight in 10% formalin, transferred to 30% sucrose in PBS for 24 h, frozen in Optimal Cutting Temperature, and kept at −80° until analysis by confocal microscopy. All fluorescent images were taken on a Zeiss Confocal LSM700, using a 20×/0.8 M27 Plan-Apochromat

objective, after mounting with Invitrogen Prolong Glass Anti-fade Mounting solution. Tile scanning was performed as well as Z-stacking for image analysis using the Fiji software (Schindelin et al., 2012). Tom⁺ crypts were defined as crypts composed entirely of Tom-labeled cells.

Immunofluorescence staining for DCLK and UEA1

Optimal Cutting Temperature-embedded sections were dried, washed in PBS, and fixed for 10 min in 10% formalin. Permeabilization in 0.05% Triton X-100 in PBS was done for 20 min followed by 1 h of blocking in 3% BSA in PBS. Staining was done overnight at 4°C, followed by washes in 0.05% Triton X-100 in PBS, staining with a secondary antibody for 1 h at RT, and staining with DAPI (1 µg/ml) and mounted. All fluorescent images were taken at 20× using a Zeiss Confocal LSM700. DCLK (rabbit polyclonal, ab31704; Abcam), UEA1 (L9006; Sigma-Aldrich). Secondary antibody: donkey anti-rabbit AF650 (SA5-10041; Invitrogen). Tissue sections were scanned at 20× magnification and Z stacked, and 7 × 7 tiling was performed to image a large area of tissue. Tom⁺ crypts were defined as crypts composed entirely of Tom-labeled cells. Thereafter, 10–15 Tom⁺ and 10–15 Tom[−] villi were identified, and the number of UEA1⁺ cells was counted.

Immunophenotyping

The distal 10 cm of the ileum was used to extract lamina propria cells as previously described (Gentile et al., 2020). For the PPs and MLNs, tissue was crushed in cold HBSS buffer (HBSS supplemented with 2% FBS and 15 mM HEPES), passed through a 100-µm filter, and centrifuged at 1,800 rpm for 5 min at 4°C. Cell suspensions were incubated with a fixable Viability dye (eFluor 506; eBioscience) for 30 min at 4°C. Cells were then incubated with Fc block (10 min at 4°C), followed by staining (for 30 min at 4°C) with the following antibodies in appropriate combinations of fluorophores. From Invitrogen: B220 (RA3-6B2), CD127 (A7R34), CD62L (MEL-14), and GATA-3 (TWAJ); from BioLegend: CD45 (30F11); and from BD: CD44 (IM7), CD3 (145-2C11), and CD4 (GK1.5). For staining of intracellular proteins, cells were fixed and permeabilized with the FoxP3 Fix/Perm kit (eBioscience) according to manufacturer's instructions. Data were acquired with a LSR Fortessa (BD Biosciences) and analyzed using FlowJo software (TreeStar).

IL4C treatment

A long-acting form of IL-4 was produced by mixing 10 µg recombinant murine IL-4 (PeproTech) with 50 µg of neutralizing monoclonal antibody (clone 11.B11; BioXcell). *Clu* fate-mapping mice were injected i.v. with IL4C on days 10, 12, and 14 after *Hpb* infection and with a single 3-mg tamoxifen i.p. injection on day 12 after infection. The SI tissue as well as feces for *Hpb* egg counts were harvested on day 12 after tamoxifen injection (day 24 after *Hpb* infection).

Parasite burden and fecundity

For worm burden assessment, mice were infected with *Hpb*, and the SI was harvested 28 dpi. Adult worms were individually removed from the intestine and enumerated. To measure

parasite fecundity, feces was collected from infected mice 14 dpi, weighed, and placed in 1 ml saturated NaCl solution. The samples were vortexed and left at room temperature for 24 h and then placed at 4°C. The eggs were enumerated and normalized to the volume of the supernatant and weight of feces.

YAP immunohistochemistry

SI tissues for immunohistochemistry were fixed overnight in formalin at room temperature. Samples were then dehydrated, embedded in paraffin, and sectioned at 4 µM. After antigen retrieval (10 mM sodium citrate buffer, pH 6) and blockage of peroxidase activity in 3% H₂O₂ solution, sections were stained with an active Yap antibody (1:300; ab205270; Abcam). Detection of primary antibodies was achieved using the Dako Envision plus system.

Statistical analysis

GraphPad Prism 9 software was used to perform statistical analyses. Student's *t* test or one- or two-way ANOVA were used as appropriate. Nonparametric tests were used when the results did not fit a normal distribution.

Online supplemental material

Fig. S1 refers to Figs. 1 and 2 and shows fetal reversion of the intestinal epithelium at the luminal stage of *Hpb* infection and after *Hpb*-CM stimulation of SI organoids. Fig. S2 refers to Figs. 1, 2, and 3 and shows partial dependence of the *Hpb*-induced fetal program on the YAP-signaling pathway and its relation to IFNγ signaling. Fig. S3 refers to Fig. 5 and shows *Clu* in situ expression and *Hpb* egg burden in *Stat6*^{−/−}, *Il4ra*^{ΔIEC} mice and in WT mice after IL4C treatment. It also shows immune-phenotyping of *Stat6*^{−/−} and *Il4ra*^{ΔIEC} mice 14 dpi. Table S1 is a complete list of differentially expressed genes. Related to RNAseq data set in Fig. 2. Table S2 is the complete list of cluster defining markers. Related to scRNAseq data set in Fig. 3.

Data and materials availability

Data sets presented can be found at GEO, accession no. GSE199227.

Acknowledgments

We thank all members of the King and Gregorieff laboratories for their support and feedback in preparing this manuscript. We greatly appreciate the technical support of Marianna Orlova (McGill), Pauline Cassart (McGill), and Sarah Boissel (Montreal Clinical Research Institute) for the scRNA-seq experiments and the McGill University Health Centre Research Institute Animal Resource Division and the Histology platform. Images throughout were created using Biorender.com.

This work was supported by the Canadian Institutes of Health Research (PJT-362757 and FRN-156038). I.L. King holds a Canada Research Chair in Barrier Immunity. M. Malleshaiah holds a Fonds de recherche du Québec—Santé, Junior 1 Scholarship.

Author contributions: Conceptualization: I.L. King, A. Gregorieff, D. Karo-Atar; Methodology: I.L. King, A. Gregorieff, D.

Karo-Atar, M. Malleshaiah, L. Diatchenko, J. von Moltke; Investigation: D. Karo-Atar, T. Javkar, S. Ouladan, S. Merritt, G. Fontes, A. Rochette, L. Joumier, M. Parisien, S. Westfall, M.E. Gentile, M.K. Matheson, G.J. Fonseca; Funding acquisition: I.L. King, A. Gregorieff; Writing—original draft: I.L. King, A. Gregorieff, D. Karo-Atar; Writing—review & editing: All authors.

Disclosures: The authors declare no competing interests exist.

Submitted: 15 November 2021

Revised: 23 March 2022

Accepted: 11 July 2022

References

- Anthony, R.M., L.I. Rutitzky, J.F. Urban, M.J. Stadecker, and W.C. Gause. 2007. Protective immune mechanisms in helminth infection. *Nat. Rev. Immunol.* 7:975–987. <https://doi.org/10.1038/nri2199>
- Ayyaz, A., S. Kumar, B. Sangiorgi, B. Ghoshal, J. Gosio, S. Ouladan, M. Fink, S. Barutcu, D. Trcka, J. Shen, et al. 2019. Single-cell transcriptomes of the regenerating intestine reveal a revival stem cell. *Nature*. 569:121–125. <https://doi.org/10.1038/s41586-019-1154-y>
- Babicki, S., D. Arndt, M. Marcu, Y. Liang, J.R. Grant, A. Maciejewski, and D.S. Wishart. 2016. Heatmapper: Web-enabled heat mapping for all. *Nucleic Acids Res.* 44:W147–W153. <https://doi.org/10.1093/nar/gkw419>
- Bankhead, P., M.B. Loughrey, J.A. Fernández, Y. Dombrowski, D.G. McArt, P.D. Dunne, S. McQuaid, R.T. Gray, L.J. Murray, H.G. Coleman, et al. 2017. QuPath: Open source software for digital pathology image analysis. *Sci. Rep.* 7:16878. <https://doi.org/10.1038/s41598-017-17204-5>
- Barner, M., M. Mohrs, F. Brombacher, and M. Kopf. 1998. Differences between IL-4Rα-deficient and IL-4-deficient mice reveal a role for IL-13 in the regulation of Th2 responses. *Curr. Biol.* 8:669–672. [https://doi.org/10.1016/S0960-9822\(98\)70256-8](https://doi.org/10.1016/S0960-9822(98)70256-8)
- Butler, A., P. Hoffman, P. Smibert, E. Papalexi, and R. Satija. 2018. Integrating single-cell transcriptomic data across different conditions, technologies, and species. *Nat. Biotechnol.* 36:411–420. <https://doi.org/10.1038/nbt.4096>
- Clevers, H. 2013. The intestinal crypt, a prototype stem cell compartment. *Cell*. 154:274–284. <https://doi.org/10.1016/j.cell.2013.07.004>
- Cliffe, L.J., N.E. Humphreys, T.E. Lane, C.S. Potten, C. Booth, and R.K. Grencis. 2005. Immunology: Accelerated intestinal epithelial cell turnover: A new mechanism of parasite expulsion. *Science*:308. 1463–1465. <https://doi.org/10.1126/science.1108661>
- Coakley, G., and N.L. Harris. 2020. The intestinal epithelium at the forefront of host-helminth interactions. *Trends Parasitol.* 36:761–772. <https://doi.org/10.1016/j.pt.2020.07.002>
- Date, S., and T. Sato. 2015. Mini-gut organoids: Reconstitution of the stem cell niche. *Annu. Rev. Cell Dev. Biol.* 31:269–289. <https://doi.org/10.1146/annurev-cellbio-100814-125218>
- Dobin, A., C.A. Davis, F. Schlesinger, J. Drenkow, C. Zaleski, S. Jha, P. Batut, M. Chaisson, and T.R. Gingeras. 2013. STAR: Ultrafast universal RNA-seq aligner. *Bioinformatics*. 29:15–21. <https://doi.org/10.1093/bioinformatics/bts635>
- Drurey, C., H.T. Lindholm, G. Coakley, M.C. Poveda, S. Löser, R. Doolan, F. Gerbe, P. Jay, N. Harris, M.J. Oudhoff, and R.M. Maizels. 2021. Intestinal epithelial tuft cell induction is negated by a murine helminth and its secreted products. *J. Exp. Med.* 219:e20211140. <https://doi.org/10.1084/jem.20211140>
- Duque-Correa, M.A., F. Schreiber, F.H. Rodgers, D. Goulding, S. Forrest, R. White, A. Buck, R.K. Grencis, and M. Berriman. 2020. Development of caecaloids to study host-pathogen interactions: New insights into immunoregulatory functions of trichuris muris extracellular vesicles in the caecum. *Int. J. Parasitol.* 50:707–718. <https://doi.org/10.1016/j.ijpara.2020.06.001>
- Ezerina, D., Y. Takano, K. Hanaoka, Y. Urano, and T.P. Dick. 2018. N-acetyl cysteine functions as a fast-acting antioxidant by triggering intracellular H₂S and sulfane sulfur production. *Cell Chem. Biol.* 25:447–459.e4. <https://doi.org/10.1016/j.chembiol.2018.01.011>
- Finkelman, F.D., T. Shea-Donohue, S.C. Morris, L. Gildea, R. Strait, K.B. Madden, L. Schopf, and J.F. Urban. 2004. Interleukin-4- and interleukin-13-mediated host protection against intestinal nematode parasites. *Immunol. Rev.* 201:139–155. <https://doi.org/10.1111/j.0105-2896.2004.00192.x>
- Gentile, M.E., Y. Li, A. Robertson, K. Shah, G. Fontes, E. Kaufmann, B. Polese, N. Khan, M. Parisien, H.M. Munter, et al. 2020. NK cell recruitment limits tissue damage during an enteric helminth infection. *Mucosal Immunol.* 13:357–370. <https://doi.org/10.1038/s41385-019-0231-8>
- Gerbe, F., E. Sidot, D.J. Smyth, M. Ohmoto, I. Matsumoto, V. Dardalhon, P. Cesses, L. Garnier, M. Pouzolles, B. Brulin, et al. 2016. Intestinal epithelial tuft cells initiate type 2 mucosal immunity to helminth parasites. *Nature*. 529:226–230. <https://doi.org/10.1038/nature16527>
- Gregorieff, A., and J.L. Wrana. 2017. Hippo signalling in intestinal regeneration and cancer. *Curr. Opin. Cell Biol.* 48:17–25. <https://doi.org/10.1016/j.ccb.2017.04.005>
- Haber, A.L., M. Biton, N. Rogel, R.H. Herbst, K. Shekhar, C. Smillie, G. Burgin, T.M. Delorey, M.R. Howitt, Y. Katz, et al. 2017. A single-cell survey of the small intestinal epithelium. *Nature*. 551:333–339. <https://doi.org/10.1038/nature24489>
- Heinz, S., C. Benner, N. Spann, E. Bertolino, Y.C. Lin, P. Laslo, J.X. Cheng, C. Murre, H. Singh, and C.K. Glass. 2010. Simple combinations of lineage-determining transcription factors prime cis-regulatory elements required for macrophage and B cell identities. *Mol. Cell.* 38:576–589. <https://doi.org/10.1016/j.molcel.2010.05.004>
- Herbert, D.R., J.Q. Yang, S.P. Hogan, K. Groschwitz, M. Khodoun, A. Munitz, T. Orekov, C. Perkins, Q. Wang, F. Brombacher, et al. 2009. Intestinal epithelial cell secretion of RELM-β protects against gastrointestinal worm infection. *J. Exp. Med.* 206:2947–2957. <https://doi.org/10.1084/jem.20091268>
- Hewitson, J.P., J.R. Grainger, and R.M. Maizels. 2009. Helminth immunoregulation: The role of parasite secreted proteins in modulating host immunity. *Mol. Biochem. Parasitol.* 167:1–11. <https://doi.org/10.1016/j.molbiopara.2009.04.008>
- Horsnell, W.G., A.J. Cutler, J.C. Hoving, C.J. Hoving, H. Mearns, E. Myburgh, B. Arendse, F.D. Finkelmann, G.K. Owens, D. Erle, and F. Brombacher. 2007. Delayed goblet cell hyperplasia, acetylcholine receptor expression, and worm expulsion in SMC-specific IL-4Rα-deficient mice. *PLoS Pathog.* 3:e1. <https://doi.org/10.1371/journal.ppat.0030001>
- Kayisoglu, O., F. Weiss, C. Niklas, I. Pierotti, M. Pompaiah, N. Wallaschek, C.T. Germer, A. Wiegner, and S. Bartfeld. 2021. Location-specific cell identity rather than exposure to GI microbiota defines many innate immune signalling cascades in the gut epithelium. *Gut*. 70:687–697. <https://doi.org/10.1136/gutjnl-2019-319919>
- Khan, K.D., G. Lindwall, S.E. Maher, and A.L. Bothwell. 1990. Characterization of promoter elements of an interferon-inducible Ly-6E/A differentiation antigen, which is expressed on activated T cells and hematopoietic stem cells. *Mol. Cell Biol.* 10:5150–5159. <https://doi.org/10.1128/mcb.10.10.5150-5159.1990>
- King, I.L., and Y. Li. 2018. Host-parasite interactions promote disease tolerance to intestinal helminth infection. *Front. Immunol.* 9:2128. <https://doi.org/10.3389/fimmu.2018.02128>
- Korotkevich, G., V. Sukhov, N. Budin, B. Shpak, M.N. Artyomov, and A. Sergushichev. 2021. Fast gene set enrichment analysis. *bioRxiv*. <https://doi.org/10.1101/060012>
- Larsen, H.L., and K.B. Jensen. 2021. Reprogramming cellular identity during intestinal regeneration. *Curr. Opin. Genet. Dev.* 70:40–47. <https://doi.org/10.1016/j.gde.2021.05.005>
- Liang, H.E., R.L. Reinhardt, J.K. Bando, B.M. Sullivan, I.C. Ho, and R.M. Locksley. 2012. Divergent expression patterns of IL-4 and IL-13 define unique functions in allergic immunity. *Nat. Immunol.* 13:58–66. <https://doi.org/10.1038/ni.2182>
- McGinty, J.W., H.A. Ting, T.E. Billipp, M.S. Nadjisombati, D.M. Khan, N.A. Barrett, H.E. Liang, I. Matsumoto, and J. von Moltke. 2020. Tuft-cell-derived leukotrienes drive rapid anti-helminth immunity in the small intestine but are dispensable for anti-protist immunity. *Immunity*. 52:528–541.e7. <https://doi.org/10.1016/j.immuni.2020.02.005>
- McInnes, L., J. Healy, N. Saul, and L. Großberger. 2018. UMAP: Uniform manifold approximation and projection. *J. Open Source Softw.* 3:861. <https://doi.org/10.21105/joss.00861>
- Meyer, A.R., M.E. Brown, P.S. McGrath, and P.J. Dempsey. 2022. Injury-induced cellular plasticity drives intestinal regeneration. *Cell Mol. Gastroenterol. Hepatol.* 13:843–856. <https://doi.org/10.1016/j.jcmgh.2021.12.005>
- Moreno, Y., P.-P. Gros, M. Tam, M. Segura, R. Valanparambil, T.G. Geary, and M.M. Stevenson. 2011. Proteomic analysis of excretory-secretory products of Heligmosomoides polygyrus assessed with

- next-generation sequencing transcriptomic information. *PLoS Negl. Trop. Dis.* 5:e1370. <https://doi.org/10.1371/journal.pntd.0001370>
- Mustata, R.C., G. Vasile, V. Fernandez-Vallone, S. Strollo, A. Lefort, F. Libert, D. Monteyne, D. Pérez-Morga, G. Vassart, and M.I. Garcia. 2013. Identification of Lgr5-independent spheroid-generating progenitors of the mouse fetal intestinal epithelium. *Cell Rep.* 5:421–432. <https://doi.org/10.1016/j.celrep.2013.09.005>
- Nusse, Y.M., A.K. Savage, P. Marangoni, A.K.M. Rosendahl-Huber, T.A. Landman, F.J. de Sauvage, R.M. Locksley, and O.D. Klein. 2018. Parasitic helminths induce fetal-like reversion in the intestinal stem cell niche. *Nature.* 559:109–113. <https://doi.org/10.1038/s41586-018-0257-1>
- Ohara, T.E., M. Colonna, and T.S. Stappenbeck. 2022. Adaptive differentiation promotes intestinal villus recovery. *Dev. Cell.* 57:166–179.e6. <https://doi.org/10.1016/j.devcel.2021.12.012>
- Ouladan, S., and A. Gregorieff. 2021. Taking a step back: Insights into the mechanisms regulating gut epithelial dedifferentiation. *Int. J. Mol. Sci.* 22:7043. <https://doi.org/10.3390/ijms22137043>
- Poss, K.D., and S. Tonegawa. 1997. Reduced stress defense in heme oxygenase 1-deficient cells. *Proc. Natl. Acad. Sci. USA.* 94:10925–10930. <https://doi.org/10.1073/pnas.94.20.10925>
- Robinson, M.D., D.J. McCarthy, and G.K. Smyth. 2009. edgeR: A Bioconductor package for differential expression analysis of digital gene expression data. *Bioinformatics.* 26:139–140. <https://doi.org/10.1093/bioinformatics/btp616>
- Santos, A.J.M., Y.H. Lo, A.T. Mah, and C.J. Kuo. 2018. The intestinal stem cell niche: Homeostasis and adaptations. *Trends Cell Biol.* 28:1062–1078. <https://doi.org/10.1016/j.tcb.2018.08.001>
- Schindelin, J., I. Arganda-Carreras, E. Frise, V. Kaynig, M. Longair, T. Pietzsch, S. Preibisch, C. Rueden, S. Saalfeld, B. Schmid, et al. 2012. Fiji: An open-source platform for biological-image analysis. *Nat. Methods.* 9: 676–682. <https://doi.org/10.1038/nmeth.2019>
- Shea-donohue, T., C. Sullivan, F.D. Finkelman, K.B. Madden, S.C. Morris, J. Goldhill, V. Piñero-carrero, and J.F. UrbanJr. 2001. The role of IL-4 in Heligmosomoides polygyrus -induced alterations in murine intestinal epithelial cell function. *J. Immunol.* 167:2234–2239. <https://doi.org/10.4049/jimmunol.167.4.2234>
- de Sousa e Melo, F., and F.J. de Sauvage. 2019. Cellular plasticity in intestinal homeostasis and disease. *Cell Stem Cell.* 24:54–64. <https://doi.org/10.1016/j.stem.2018.11.019>
- Trapnell, C., D. Cacchiarelli, J. Grimsby, P. Pokharel, S. Li, M. Morse, N.J. Lennon, K.J. Livak, T.S. Mikkelsen, and J.L. Rinn. 2014. The dynamics and regulators of cell fate decisions are revealed by pseudotemporal ordering of single cells. *Nat. Biotechnol.* 32:381–386. <https://doi.org/10.1038/nbt.2859>
- Urban, J.F., C.R. Maliszewski, K.B. Madden, I.M. Katona, and F.D. Finkelman. 1995. IL-4 treatment can cure established gastrointestinal nematode infections in immunocompetent and immunodeficient mice. *J. Immunol.* 154:4675–4684
- Valanparambil, R.M., M. Segura, M. Tam, A. Jardim, T.G. Geary, and M.M. Stevenson. 2014. Production and analysis of immunomodulatory excretory-secretory products from the mouse gastrointestinal nematode Heligmosomoides polygyrus bakeri. *Nat. Protoc.* 9:2740–2754. <https://doi.org/10.1038/nprot.2014.184>
- von Moltke, J., M. Ji, H.E. Liang, and R.M. Locksley. 2016. Tuft-cell-derived IL-25 regulates an intestinal ILC2–epithelial response circuit. *Nature.* 529:221–225. <https://doi.org/10.1038/nature16161>
- Yui, S., L. Azzolin, M. Maimets, M.T. Pedersen, R.P. Fordham, S.L. Hansen, H.L. Larsen, J. Guiu, M.R.P. Alves, C.F. Rundsten, et al. 2018. YAP/TAZ-Dependent reprogramming of colonic epithelium links ECM remodeling to tissue regeneration. *Cell Stem Cell.* 22:35–49.e7. <https://doi.org/10.1016/j.stem.2017.11.001>
- Zhou, Y., B. Zhou, L. Pache, M. Chang, A.H. Khodabakhshi, O. Tanaseichuk, C. Benner, and S.K. Chanda. 2019. Metascape provides a biologist-oriented resource for the analysis of systems-level datasets. *Nat. Commun.* 10: 1523. <https://doi.org/10.1038/s41467-019-09234-6>

Supplemental material

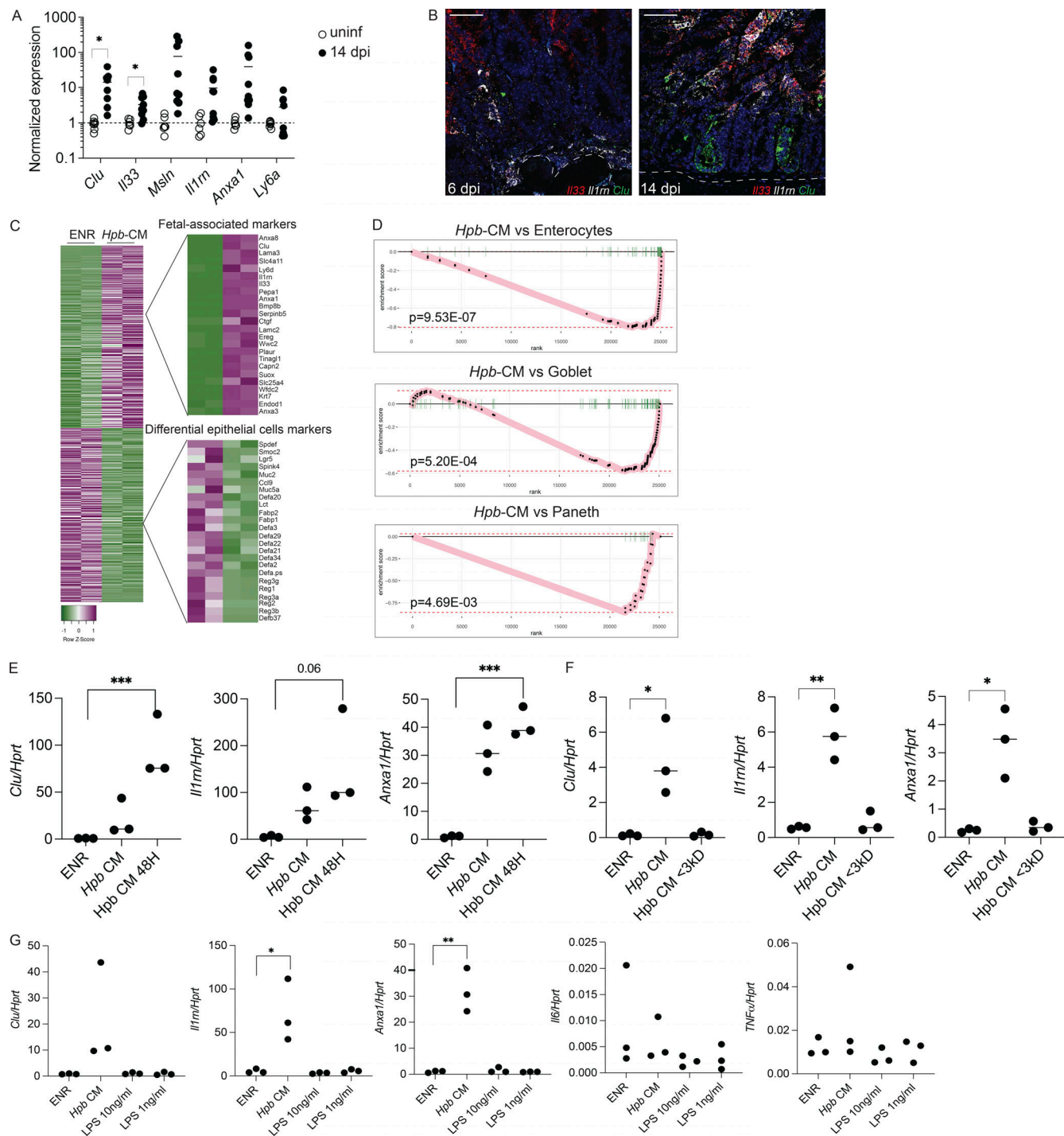


Figure S1. Fetal reversion of the intestinal epithelium at the luminal stage of *Hpb* infection and following *Hpb*-CM stimulation of SI organoids. Related to Figs. 1 and 2. **(A)** Epithelial cells were extracted from the SI of uninfected mice on day 14 after *Hpb* infection, and expression of the indicated fetal genes was assessed by qPCR. **(B)** RNAscope of *Il33*, *Il1rn*, and *Clu* on days 6 and 14 after *Hpb* infection of SI tissues. **(C)** Heatmap of reads per kilobase million was created using the Heatmapper web tool (Babicki et al., 2016). **(D)** GSEA of transcripts associated with mature enterocytes, goblet cells, and Paneth cells following *Hpb*-CM stimulation of organoids. To exclude the possibility of endotoxin or host protein contamination in *Hpb*-CM, the following three experiments were performed: **(E)** *Hpb* adult worms were incubated in organoid basal medium. 24 h later, CM was collected (*Hpb*-CM), and the worms were moved into fresh organoid basal medium for an additional 24 h. At the 48-h time point, CM was collected again (*Hpb*-CM 48H). SI organoids were stimulated on day 0 of culture with *Hpb*-CM, *Hpb*-CM 48H, or control ENR medium. qPCR analysis of selected fetal-associated genes is shown. **(F)** *Hpb*-CM was passed through a 3-kD filter, and the flowthrough was collected. SI organoids were stimulated on day 0 of culture with crude *Hpb*-CM, flowthrough fraction of *Hpb*-CM (*Hpb*-CM <3 kD), or control ENR medium. **(G)** SI organoids were stimulated on day 0 of culture with *Hpb*-CM, 1 ng/ml LPS, 10 ng/ml LPS, or control ENR medium. qPCR analysis of selected fetal-associated genes as well as *Il6* and *Tnfa* is shown. Scale bar, 50 μ m. Data shown are representative of two independent experiments (A, B, and E–G) or one independent experiment (C and D), $n > 3$ biological replicates. Statistical tests: t test (A–G); *, $P < 0.05$; **, $P < 0.01$; ***, $P < 0.005$.

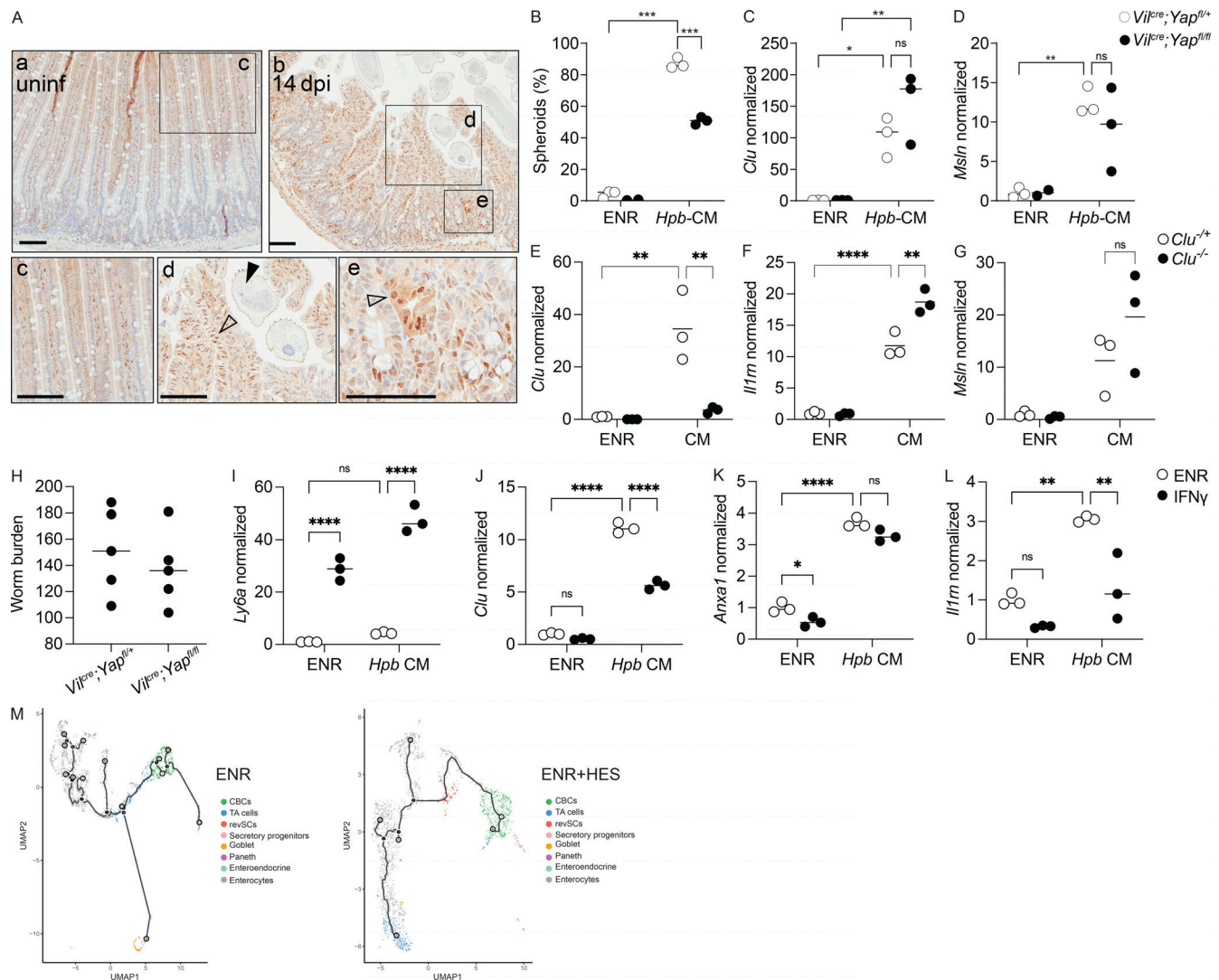


Figure S2. Fetal-like reprogramming is partially Yap dependent and is not amplified by IFN γ . Related to Figs. 1, 2, and 3. **(A)** Immunohistochemistry for active YAP; squares, area in bottom panel; open arrowheads, nuclear YAP expression; black arrowheads, worm presence. **(B–D)** qPCR analysis of the indicated genes from *Yap^{-/-}* and littermate control SI organoids stimulated with *Hpb*-CM for 24 h. **(E–G)** qPCR analysis of *Clu^{-/-}* and littermate control SI organoids stimulated with *Hpb*-CM for 24 h. **(H–K)** *Yap^{fl/fl}* and littermate control *Yap^{fl/fl}* mice were infected with 150 L3 *Hpb* larvae, and adult worms were counted 28 dpi. **(I–K)** qPCR analysis of the indicated genes from SI organoids stimulated, on day 0 of culture, with ENR (control) or 10 ng/ml IFN γ with or without *Hpb*-CM for 24 h. **(M)** Monocle 3 direct exports of the trajectory analysis using CBCs as the pseudotime source variable, showing the distribution of the different cell clusters along the pseudotime variable. Scale bar, 100 μ m. Data shown are representative of two or more independent experiments, $n > 3$ biological replicates; statistical tests: two-way ANOVA (B–L); *, $P < 0.05$; **, $P < 0.01$; ***, $P < 0.005$; ****, $P < 0.001$.

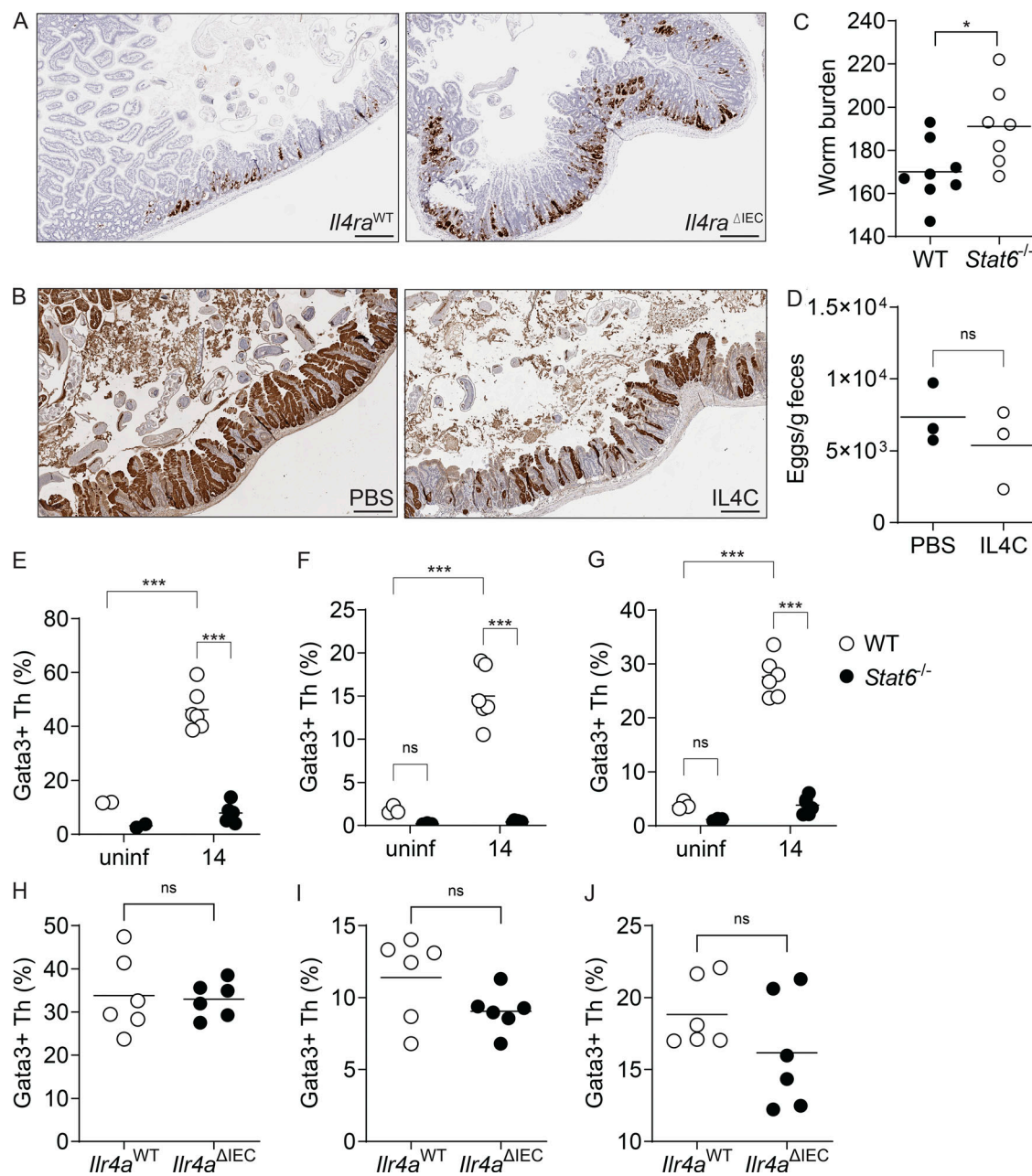


Figure S3. **A balanced regulation of the ISC niche by helminths and type 2 immune signaling supports durable infection.** Related to Fig. 5. **(A)** Representative photomicrographs of *Clu* RNAscope of *Il4ra*^{WT} and *Il4ra*^{ΔIEC} tissue sections on day 14 after *Hpb* infection. **(B)** Representative photomicrographs of dtTomato expression in *Clu* fate-mapping mice treated with PBS or IL4C as described in Fig. 5 Q and Materials and methods. **(C)** *Hpb* worm burden 28 dpi in WT and *Stat6*^{-/-} mice. **(D)** *Hpb* egg burden following IL4C treatment. **(E–J)** Immune phenotyping on day 14 after *Hpb* infection. SI (E), PPs (F), and MLNs (G) were harvested from WT and *Stat6*^{-/-} mice. Single-cell suspensions were made, and flow cytometry was performed. Cells were gated for viable CD45⁺CD3⁺B220⁻CD4⁺CD62L⁻CD44^{high} cells, and Gata3⁺ cells were identified as Th2 cells. Percentage of Gata3⁺ cells of the CD62L⁻CD44⁺ population. **(H–J)** SI (H), PPs (I), and MLN (J) were harvested from *Il4ra*^{WT} and *Il4ra*^{ΔIEC} mice. Single-cell suspensions were made, and flow cytometry was performed. Cells were gated for viable CD45⁺CD3⁺B220⁻CD4⁺CD62L⁻CD44^{high} cells, and Gata3⁺ cells were identified as Th2 cells. Percentage of Gata3⁺ cells of the CD62L⁻CD44⁺ population. Scale bar, 500 μm. Data shown are representative of two or more independent experiments, *n* = 6 biological replicates; statistical tests: *t* test (C, D, and H–J); two-way ANOVA (E–G); *, *P* < 0.05; ***, *P* < 0.005.

Provided online are two tables. Table S1 is a complete list of differentially expressed genes. Related to RNAseq data set in Fig 2. Table S2 is the complete list of cluster defining markers. Related to scRNAseq data set in Fig 3.